Supplementary Information (SI) for Journal of Materials Chemistry A.

Slow-Light Enhanced Photocatalytic Water Splitting over Cu-Incorporated 3D Ordered Macroporous ZIF-8

Junzhou Men [a], Zeyu Wang [a], Chen Luo [a], Ai Zhang [a], Hui Xian [c], Tao Jiang [a,], Yating Wang [a,b,*]*

[a] Tianjin Key Laboratory of Brine Chemical Engineering and Resource Eco-utilization, Tianjin Key Laboratory of Multiplexed Identification for Port Hazardous Chemicals, School of Chemical Engineering and Material Science, Tianjin University of Science & Technology, Tianjin 300457, P. R. China.

[b] National Engineering Research Center of Distillation Technology, Collaborative Innovation Center of Chemical Science and Engineering (Tianjin), School of Chemical Engineering and Technology, Tianjin University, Tianjin 300072, P. R. China.

[c] School of Continuing Education, Tiangong University, Tianjin 300387, P. R. China.

*Corresponding author: wangyating@tust.edu.cn; jiangtao@tust.edu.cn

Catalogue

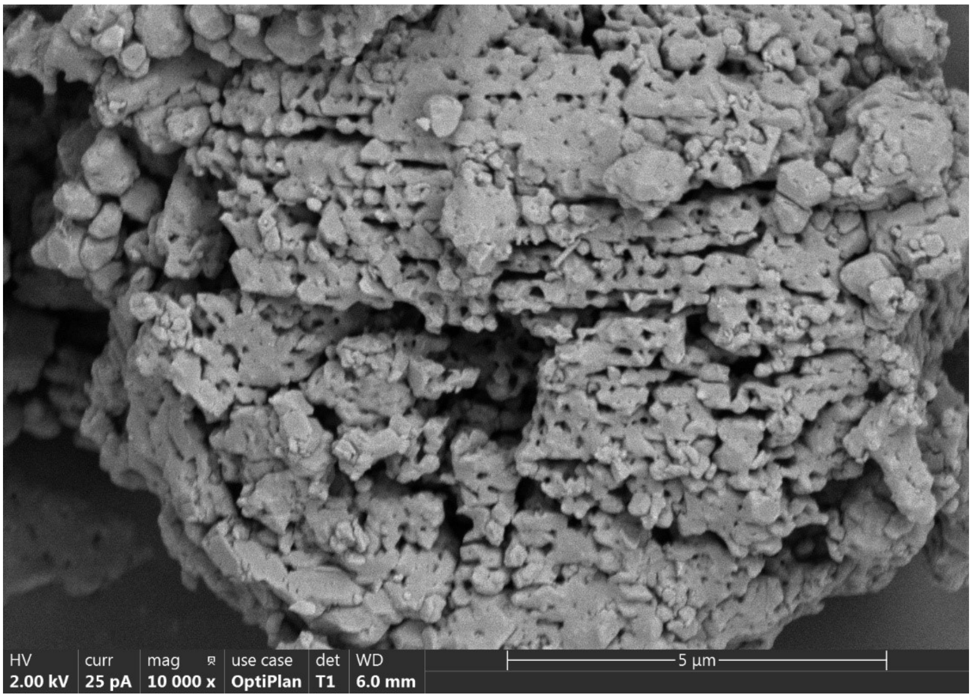

Fig. S1 The SEM image of Cu-3D-ZIF-248 with reduced PS template content (RCu-3D-ZIF-8-248) was magnified by 10000 times.

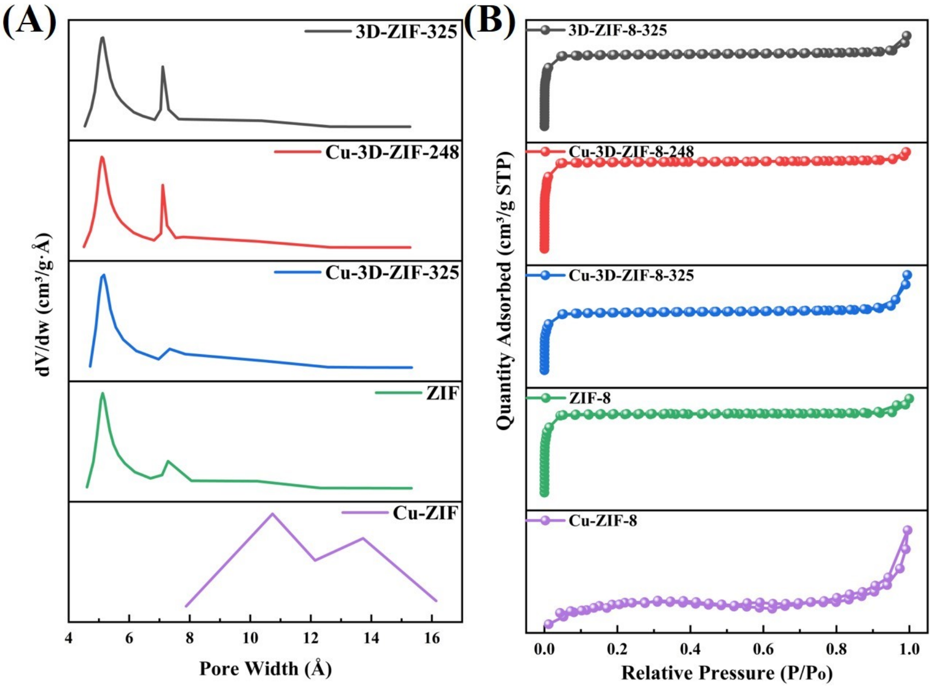

Fig. S2 (A) The pore size distribution and(B) N_2 adsorption-desorption isotherms of as-prepared samples.

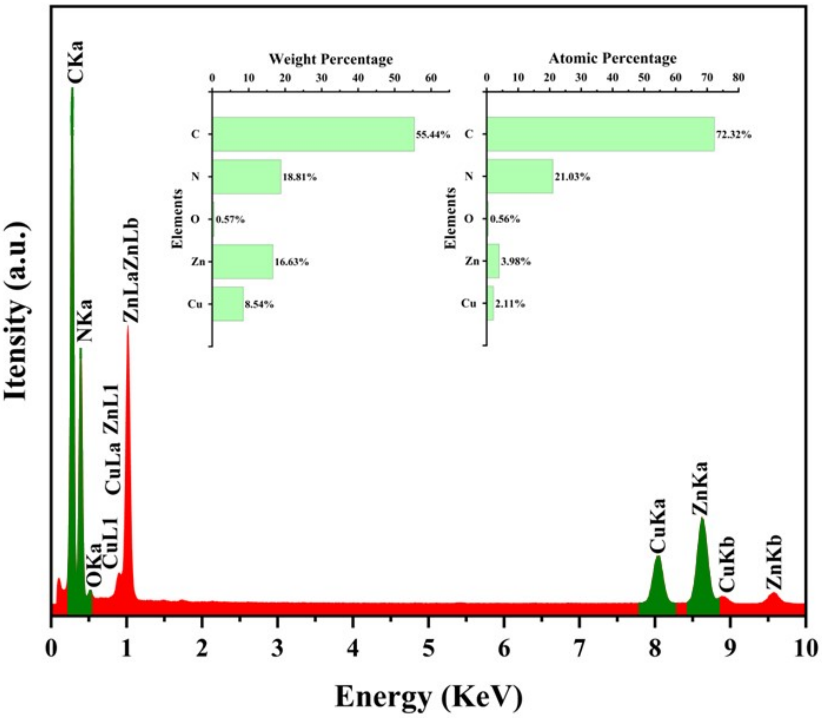

Fig. S3 The element mapping of Cu-3D-ZIF-325.

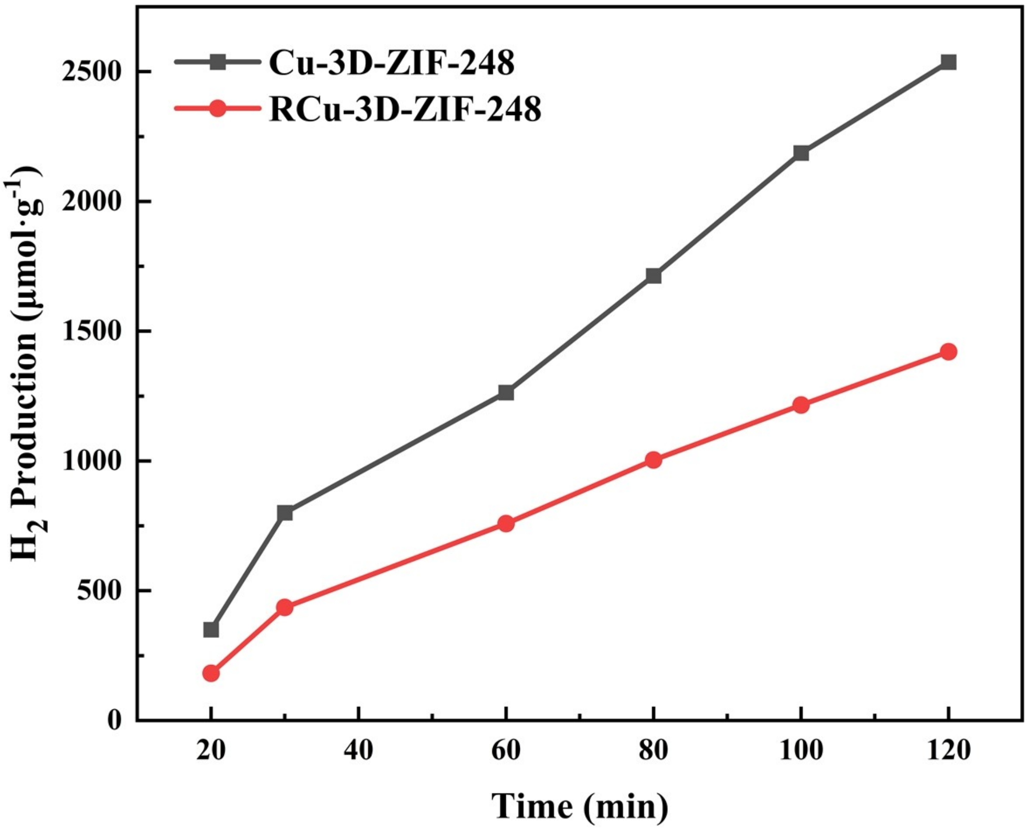

Fig. S4 The efficiencies of hydrogen generation over Cu-3D-ZIF-248 and RCu-3D-ZIF-248 under simulated sunlight irradiation

Table S1 The weight loss of as-prepared samples in TG.

Weight loss (%)	Cu-ZIF	ZIF	Cu-3D-ZIF-325	Cu-3D-ZIF-248	3D-ZIF-325
Stage I	18.54	4.14	6.93	4.93	8.64
Stage II	4.98	5.80	8.76	7.80	8.52
Stage III	48.11	55.63	49.94	55.62	51.17
Residual mass	27.37	34.43	34.47	32.25	31.67

Table S2 The PS diameter, pore size and shrinkage.

Sample name	Template diameter (nm)	Average pore size (nm)	Shrinkage rate %
Cu-3D-ZIF-248	248	221	10.89
Cu-3D-ZIF-325	325	315	3.1
3D-ZIF-325	325	312	4

Table S3 The specific surface area and pore structure of the samples.

samples	Cu-ZIF	ZIF	Cu-3D-ZIF-325	Cu-3D-ZIF-248	3D-ZIF-325
pore diameter (Å)	35.99	16.29	17.33	16.42	17.26
Average pore size of mesopores (Å)	57.39	131.06	246.93	109.17	143.47
micropore volume (cm^3/g)	0.00	0.06	0.33	0.64	0.56
Mesoporous pore volume (cm^3/g)	0.00	0.40	0.06	0.04	0.06
total pore volume(cm^3/g)	0.00	0.46	0.39	0.68	0.62
specific surface area (m^2/g)	1.15	1141.39	896.05	1660.78	1441.75

Table S4 The proportions of various elements in the XPS survey spectrum of as-prepared samples

Samples	C/at%	N/at%	O/at%	Zn/at%	Cu/at%
Cu-ZIF	58.87	27.82	6.29	6.81	0.22
ZIF	58.21	28.19	5.79	7.81	--
Cu-3D-ZIF-325	60.87	26.94	4.64	7.31	0.24
Cu-3D-ZIF-248	64.25	24.32	5.10	6.13	0.20
3D-ZIF-325	61.81	27.03	4.18	6.98	--

Table S5 The peak proportion of C 1s XPS spectra of as-prepared samples.

Samples	Peak position (eV)			Peak area ratio (%)		
	C-O	C-N	C=C	C-O	C-N	C=C
Cu-ZIF	291.80	286.00	284.70	3.95%	28.34%	67.71%
ZIF	291.81	286.02	284.71	3.89%	30.53%	65.58%
Cu-3D-ZIF-325	291.81	286.01	284.72	3.23%	26.03%	70.74%
Cu-3D-ZIF-248	291.80	286.00	284.71	3.66%	24.32%	72.02%
3D-ZIF-325	291.81	286.02	284.70	2.96%	28.18%	68.87%

Table S6 The peak proportion of N 1s XPS spectra of as-prepared samples.

Samples	Peak position (eV)		Peak area ratio (%)	
	N-Zn/Cu	C-N	N-Zn/Cu	C-N
Cu-ZIF	400.40	398.70	6.57%	93.43%
ZIF	400.42	398.73	4.18%	95.82%
Cu-3D-ZIF-325	400.41	398.72	5.47%	94.53%
Cu-3D-ZIF-248	400.43	398.87	8.33%	91.67%
3D-ZIF-325	400.40	398.71	6.83%	93.17%

Table S7 The peak proportion of O 1s XPS spectra of as-prepared samples.

Samples	Peak position (eV)		Peak area ratio (%)	
	O-H	C-O	O-H	C-O
Cu-ZIF	531.95	531.15	43.32%	56.68%
ZIF	531.95	531.15	40.71%	59.29%
Cu-3D-ZIF-325	531.94	531.15	40.63%	59.37%
Cu-3D-ZIF-248	531.29	531.07	39.00%	61.00%
3D-ZIF-325	531.94	531.16	40.49%	59.51%

Table S8 The peak proportion of Zn 2p XPS spectra of as-prepared samples.

Samples	Peak position (eV)		Peak area ratio (%)	
	$2p_{1/2}$	$2p_{3/2}$	$2p_{1/2}$	$2p_{3/2}$
Cu-ZIF	1044.80	1021.72	33.32%	66.68%
ZIF	1044.81	1021.72	33.33%	66.67%
Cu-3D-ZIF-325	1044.82	1021.72	33.34%	66.66%
Cu-3D-ZIF-248	1044.82	1021.70	33.33%	66.67%
3D-ZIF-325	1044.81	1021.72	33.30%	66.70%

Table S9 The peak proportion of Cu 2p XPS spectra of as-prepared samples.

Samples	Peak position (eV)		Peak area ratio (%)	
	2p1/2	2p3/2	2p1/2	2p3/2
Cu-ZIF	953.90	933.11	33.34%	66.66%
Cu-3D-ZIF-325	953.90	933.13	33.33%	66.67%
Cu-3D-ZIF-248	953.49	933.46	33.33%	66.67%

Table S10 The apparent quantum efficiency of the sample

Sample	Cu-ZIF	ZIF	Cu-3D-ZIF-325	Cu-3D-ZIF-248	3D-ZIF-325
Apparent quantum efficiency	3.17	0.40	11.72	6.77	0.43

Table S11 The kinetic constants extracted from the time-resolved PL decay curves of samples Cu-ZIF, ZIF, Cu-3D-ZIF-325, Cu-3D-ZIF-248 and 3D-ZIF-325 were calculated by fitting.

Samples	τ_1(ns)	Rel_1(%)	τ_2(ns)	Rel_2(%)	$\tau_{(avg)}$ (ns)
Cu-ZIF	2.56	69.64	19.49	30.36	7.70
ZIF	1.75	71.13	4.02	28.87	2.41
Cu-3D-ZIF-325	1.39	58.20	5.79	41.80	3.23
Cu-3D-ZIF-248	1.61	59.97	6.72	40.03	3.65
3D-ZIF-325	1.96	63.88	5.94	36.12	3.39

Table S12 Previously reported photocatalytic hydrogen evolution performance and apparent quantum efficiency (AQE) of advanced MOF-based photocatalysts.

Samples	H_2 Production Rate (umol·g^{-1}·h^{-1})
Pd@MOF-808-b [1]	236
Cu-MOF/$ZnIn_2S_4$-10 [2]	300
PbS/NTU-9 [3]	432
Fe-MOF-525 [4]	505.4
MoS_2@Cu/Co-MOF [5]	832.4
Co-MOF/H-g-C_3N_4 [6]	1033
ZrO_2/Zr-MOF/Pt [7]	1327
ZCS@$Cu_{0.75}$/Fe-MOF [8]	1563.96
this work	2233.20

Table S13 The photocatalytic hydrogen evolution performance and apparent quantum efficiency (AQE) of advanced photocatalysts have been previously reported.

Samples	H_2 Production Rate (umol·g^{-1}·h^{-1})	Apparent quantum efficiency (%)	Wavelength (nm)
Co-Co PBA/GDY [9]	96.93	1.94	470
CdS/MoC[10]	224.5	7.6	420
Na-SPHI [11]	571.8	61.7	420
g-C_3N_4 (CN_3) [12]	1160	7.67	420
CuPtAu/g-C_3N_4[13]	1451	4.9	370
CoS/g-C_3N_4/NiS[14]	1930	16.4	420
This work	2233.20	11.72	400

In this study, Cu^{2+} doping achieves a significant amplification of the slow light effect by precisely regulating the refractive index (*n*) and photonic band gap (PBG) characteristics of 3DOM ZIF-8, with the underlying mechanism elaborated as follows:

Firstly, Cu^{2+} doping effectively increase the dielectric constant (ε) of the ZIF-8 solid phase This is attributed to the partial substitution of Zn^{2+} by Cu^{2+} in the ZIF-8 lattice, where Cu^{2+} forms a stable coordination environment. For non-magnetic materials, the refractive index and dielectric constant follow the relationship $n = \sqrt{\mu\varepsilon}$ (where μ is the magnetic permeability, approximately a constant), leading to a direct increase in the refractive index (*n*) of the ZIF-8 solid phase upon Cu^{2+} doping. The enhanced n significantly promotes multiple scattering and total internal reflection of light within the 3DOM macropores, prolonging the light residence time inside the catalyst and thereby amplifying the slow light effect.

Secondly, Cu^{2+} doping modulates the PBG position by increasing n. The PBG can be easily calculated according to the modified Bragg's law (Chem, 2 (2017) 877-892.):

$$\lambda = 2\sqrt{\frac{2}{3}}D\sqrt{n_{ZIF-8}^{2}f + n_{void}^{2}(1-f) - \sin^{2}\theta}$$

λ is the wavelength associated with the photonic band gap, D is the macropore diameter of 3DOM ZIF-8 (Table S2), n is the refractive index; f is the volume fraction of ZIF-8, typically taken as 0.4; θ is the incident angle of light.

When $\theta = 0°$, the PBG wavelength (λ) depends exclusively on the macropore diameter (D) and the effective refractive index of 3DOM ZIF-8. Notably, the measured PBG wavelength ($\lambda_{\text{measured}}$) from reflection spectra exhibits excellent agreement with the calculated value ($\lambda_{\text{calculated}}$) using the modified Bragg's law. As indicated by the equation, a larger macropore diameter (D) or higher refractive index (n) results in a longer PBG wavelength, thereby expanding the PBG range. Thus, the enhancement of n induced by Cu^{2+} doping further promotes the expansion of the PBG.

In summary, Cu^{2+} doping enhances the solid-phase refractive index by increasing the dielectric constant of ZIF-8, which strengthens light scattering and extends the optical path length. Consequently, the slow light effect of Cu-3D-ZIF-325 is significantly superior to that of pristine 3D-ZIF-8, ultimately leading to substantial improvements in light harvesting efficiency and photocatalytic hydrogen evolution activity.

Table S14 The diameters of PS spheres, the pore diameter and the photonic band gap positions measured by reflectance spectra and calculated by the modified Bragg's law.

Sample name	PS diameter (nm)	Pore diameter (nm)	Shrinkage %	$\lambda_{\text{measured}}$	$\lambda_{\text{calculated}}$
Cu-3D-ZIF-248	248	221	10.89	559	562
Cu-3D-ZIF-325	325	315	3.1	592	588

Introduction to DFT calculations

All theoretical calculations were performed using the Vienna Ab-initio Simulation Package (VASP). The electron exchange-correlation interactions were described by the generalized gradient approximation (GGA) combined with the Perdew-Burke-Ernzerhof (PBE) potential. The electronic wave functions were expanded using a plane-wave basis set with a cutoff energy of 520 eV, and the interlayer van der Waals interactions were corrected via Grimme's DFT-D3 method. For k-point sampling in the first Brillouin zone, the Γ-centered Monkhorst-Pack scheme was adopted with a grid setting of 2×2×1. The convergence criteria for structural optimization were set as follows: the force acting on each atom in the model was less than 0.03 $eV \cdot Å^{-1}$, and the total energy of the system converged to 10^{-5} eV. Meanwhile, to avoid spurious interactions between periodic repeating units, a vacuum layer larger than 15 Å was set along the z-direction (crystallographic direction), a treatment widely employed in the local structural simulation of porous framework materials.In the DFT calculations, the structural model of ZIF-8 was directly taken from the experimentally reported unit cell without further simplification, with lattice constants of 16.99 Å×16.99 Å×16.99 Å. This unit cell was fully optimized and served as the basis for constructing the calculation model. To balance the approximate simulation of the local environment of the 3DOM framework and computational feasibility, a slab model was built based on this optimized unit cell. The resulting structure is consistent with the modeling strategies reported in recent studies on 3DOM ZIF-8 frameworks, and this periodic repeating fragment can provide reliable and physically meaningful characterization of local structural features for the adsorption and reaction analyses involved in this work.

Reference

[1] J. Xu, J. Liu, Z. Li, X. Wang, Z.J.J.o.M.S. Wang, Synthesis, structure and properties of Pd@ MOF-808, J. Mater. Sci, 54 (2019) 12911-12924.

[2] H. Chen, J. Wu, Y. Zhu, J. Yang, B. Tang, T. Zhang, H.J.R.E. Yang, Cu-MOF modified ZnIn2S4 nanosheet composite catalyst for photocatalytic hydrogen production, Renewable Energy, 228 (2024) 120672.

[3] R. Kaur, V.A. Chhabra, A. Rana, R.K. Singh, S. Tripathi, K.-H. Kim, A.J.I.J.o.H.E. Deep, QD/MOF nanocomposites as novel photoanode for photocatalytic and photovoltaic applications, Int. J. Hydrog. Energy, 107 (2025) 63-73.

[4] Y. Wu, Y. Qu, C. Su, X. Yang, Y. Yang, Y. Zhang, W.J.I.C. Huang, Enhanced photoinduced carrier separation in Fe-MOF-525/CdS for photocatalytic hydrogen evolution: improved catalytic dynamics with specific active sites, Inorg. Chem, 62 (2023) 21290-21298.

[5] D. Masekela, T.L. Yusuf, S.A. Balogun, E. Makhado, O.I. Adeniran, K.D.J.J.o.A. Modibane, Compounds, Interfacial engineering of MoS_2 and bimetallic MOF hybrid for superior piezo-photocatalytic hydrogen production and wastewater treatment, J. Alloy. Compd, 1020 (2025) 179304.

[6] Z. Liu, J. Xu, T. Xue, X. Liu, S. Xu, Z.J.N.J.o.C. Li, Hydrogen evolution performance of Co-MOF/Hg-C_3N_4 composite catalysts with different morphologies under visible light, New J. Chem, 47 (2023) 3703-3713.

[7] W.W. Cheng, S.N. Zhang, J. Wang, J. Yang, Z. Yang, X.F. Chen, J.D. Xiao, J.J.C.A.E.J. Wang, Boosting Hydrogen Production of a MOF-based Multicomponent Photocatalyst with Clean Interface via Facile One-pot Electrosynthesis, Chem. Eur J, 30 (2024) e202303886.

[8] B. Zhao, J. Liu, Y. Liu, W. Wen, Z.J.J.o.A. Li, Compounds, In situ growth of ZnCdS nanoparticles on bimetallic Cu/Fe-MOF for efficient visible-light-driven photocatalytic hydrogen production and urea synthesis, J. Alloy. Compd, 1011 (2025) 178395.

[9] K. Wang, M. Wang, H. Xie, S. Li, X. Kong, Z.J.S. Jin, P. Technology, Rational construction of graphdiyne (g-CnH2n− 2) coupling with Co-Co PBA S-scheme heterojunctions for efficient photocatalytic hydrogen production, Sep. Purif. Technol., 322 (2023) 124286.

[10] Y. Lei, X. Wu, S. Li, J. Huang, K.H. Ng, Y.J.J.o.C.P. Lai, Noble-metal-free metallic MoC combined with CdS for enhanced visible-light-driven photocatalytic hydrogen evolution, J. Clean. Prod., 322 (2021) 129018.

[11] Y. Li, D. Ge, H. Zhang, L. Shangguan, Z. Mou, F. Xia, J. Sun, X. Liu, Y. Su, W.J.S. Lei, Solvated Electrons Generated on the Surface of Na-SPHI for Boosting Visible Light Photocatalytic Hydrogen Evolution with Ultra-High AQE, Small, 20 (2024) 2401392.

[12] J. Huang, Y. Cao, H. Wang, H. Yu, F. Peng, H. Zou, Z.J.C.E.J. Liu, Revealing active-site structure of porous nitrogen-defected carbon nitride for highly effective photocatalytic hydrogen evolution, Chem. Eng. J., 373 (2019) 687-699.

[13] L. Zhang, Y. Zang, J. Ren, Y. Xue, J.J.I.J.o.H.E. Tian, Medium-entropy design boosts photocatalytic hydrogen production on g-C3N4, Int. J. Hydrog. Energy, 166 (2025) 151021.

[14] Z.-x. Bi, R.-t. Guo, X.-y. Ji, X. Hu, J. Wang, X. Chen, W.-g.J.I.J.o.H.E. Pan, Direct Z-scheme CoS/g-C3N4 heterojunction with NiS co-catalyst for efficient photocatalytic hydrogen generation, Int. J. Hydrog. Energy, 47 (2022) 34430-34443.